Journal of
Materials Chemistry A

ROYAL SOCIETY
OF CHEMISTRY

PAPER

View Article Online
View Journal

Check for updates

Cite this: DOI: 10.1039/d6ta00038j

Mechanochemically engineered defect-rich Zn/Co-ZIF-8 solid solutions for enhanced electrochemical water splitting

Priyanka Kumari,†[b] Abdul Kareem, †[b] Mebin Varghese,[b] Arjun Warrier, [b]
Sellappan Senthilkumar [b] and Tamas Panda *[a]

Received 3rd January 2026
Accepted 9th April 2026

DOI: 10.1039/d6ta00038j

rsc.li/materials-a

Zeolitic imidazolate frameworks (ZIFs), a subclass of porous MOFs, have attracted significant attention due to their high crystallinity and exceptional thermal and chemical stability. The synthetic protocols of Zn-ZIF-8 and Co-ZIF-8 strongly influence their thermodynamic and kinetic properties. Room-temperature (RT) aqueous synthesis yields less crystalline phases (pZn-ZIF-8-RT and pCo-ZIF-8-RT) compared to high-temperature (HT) solvothermal synthesis in DMF/DEF (pZn-ZIF-8-HT and pCo-ZIF-8-HT). Mechanical milling of equimolar RT-synthesized phases produces a highly disordered amorphous solid solution, a-$Zn_{50}Co_{50}$ZIF8-RT, which upon water/methanol vapor exposure at 25 °C transforms into a crystalline counterpart (c-$Zn_{50}Co_{50}$ZIF8-RT). Following the same protocol, milling of HT-synthesized precursors yields a more ordered amorphous phase, a-$Zn_{50}Co_{50}$ZIF8-HT. Comprehensive characterization using DFT, Raman spectroscopy, FE-SEM, and HR-TEM reveals that a-$Zn_{50}Co_{50}$ZIF8-RT possesses abundant active sites, enhanced electron density, and a less ordered structure, making it an efficient electrocatalyst. Consequently, it exhibits superior performance towards electrocatalytic water splitting with low overpotentials of 301 mV (OER) and 437 mV (HER) at 10 mA cm^{-2}, outperforming that of a-$Zn_{50}Co_{50}$ZIF8-HT, c-$Zn_{50}Co_{50}$ZIF8-RT and c-$Zn_{50}Co_{50}$ZIF8-HT.

Introduction

Electrochemical water splitting is widely recognized as a sustainable pathway for hydrogen production, offering a clean alternative to fossil fuel based methods.[1] This involves hydrogen generation at the cathode *via* the hydrogen evolution reaction (HER) and oxygen production at the anode through the oxygen evolution reaction (OER). These reactions present a promising strategy to enhance energy security, overcome storage challenges, and mitigate carbon emissions.[2] Noble metal catalysts such as Pt, Pd, IrO_2, and RuO_2 remain as benchmarks for the HER and OER due to their low overpotentials and high activity. However, their scarcity and high cost restrict the scalability, which emphasize the urgent need for earth-abundant and cost-effective alternatives.[3–6] Transition-metal-based catalysts, including oxides, hydroxides, phosphides, sulfides, and more recently metal organic frameworks (MOFs), have emerged as promising substitutes. MOFs, in particular, are attractive because of their structural tunability, high surface area, and versatile composition.[7–13] Despite these advantages, many pristine MOFs lack stability in alkaline media, which limits their catalytic application in electrochemical water splitting. Mitigating this limitation necessitates the development of innovative design approaches that effectively balance the crystallinity, disorder, and electronic structure.

Within the MOF family, zeolitic imidazolate frameworks (ZIFs) stand out due to their robust topology, high porosity, and superior chemical and thermal stability.[14–17] Yaghi and co-workers first reported ZIF-8 synthesis under solvothermal conditions in *N*,*N*-dimethylformamide (DMF), achieving highly crystalline materials with large surface area and micropore volume.[18] However, the reliance on high-boiling, toxic organic solvents such as DMF and diethylformamide (DEF) poses challenges for large-scale synthesis and environmental sustainability. Consequently, water-based, room-temperature (RT) methods have been developed as greener alternatives.[19] These approaches not only eliminate hazardous solvents but also enable faster nucleation and higher yields. Interestingly, the choice of solvent greatly influences the crystal growth: while RT synthesis using water can produce ZIF-8 at specific metal/ligand ratios, the same synthesis fails under similar conditions in DMF. Conversely, high-temperature solvothermal synthesis in DMF produced good ZIF-8 crystals, but the same synthesis does not succeed in water.[20–24] These observations

---

[a] *Centre for Clean Environment, Vellore Institute of Technology, Vellore, Tamil Nadu – 632014, India. E-mail: tamaskumarpanda@vit.ac.in*

[b] *Department of Chemistry, School of Advanced Sciences, Vellore Institute of Technology, Vellore, Tamil Nadu – 632014, India*

† PK and AK contributed equally to this work.

signify the critical role of synthetic protocols in governing both the crystallinity and catalytic activity of MOFs/ZIFs.[21–26]

As an alternative to the conventional solution-based synthesis,[27,28] mechanochemical approaches have recently gained attraction as an efficient, solvent-free strategy for producing ZIF and MOF solid solutions. This eco-friendly technique offers precise control over crystallinity, porosity and the local electronic environment of active sites, often yielding enhanced catalytic activity and stability. Our earlier work demonstrated that mechanically milled solid solutions of Zn-ZIF-8 and Co-ZIF-8 outperform their pristine precursors in photocatalytic dye degradation. Furthermore, we revealed that the amorphous solid solution phase (a-$Zn_{50}Co_{50}$ZIF8) exhibits superior performance compared to its crystalline counterpart, highlighting the beneficial role of structural disorder.[29]

Based on these observations, we envisage that tuning the degree of disorder in ZIF-based solid solutions could enhance the electrocatalytic performance. In this work, we establish a strategy to regulate the disorder by suitably varying the synthetic route of precursors prior to mechanochemical processing. Specifically, RT aqueous synthesis of Zn-ZIF-8 and Co-ZIF-8, followed by mechanical milling, yields a highly disordered amorphous solid solution, a-$Zn_{50}Co_{50}$ZIF8-RT. In contrast, HT solvothermal synthesis in DMF, combined with mechanical milling, produces a comparatively ordered amorphous solid solution phase, a-$Zn_{50}Co_{50}$ZIF8-HT. Strikingly, the more defective and disordered a-$Zn_{50}Co_{50}$ZIF8-RT exhibits enhanced HER and OER activities, significantly outperforming its less disordered HT-derived analogue.

To the best of our knowledge, this is the first investigation to demonstrate how variations in synthetic protocols of ZIF precursors can be exploited to modulate the structural disorder in amorphous solid solutions, thereby maximizing their catalytic activity. These findings not only provide fundamental insights into structure–property relationships in ZIFs but also establish a new direction for designing low-cost, efficient and durable electrocatalysts for overall water splitting.

Results and discussion

The method used for the synthesis of ZIF precursors can be exploited to modulate the structural disorder in amorphous solid solutions, thereby maximizing their reaction kinetics, excellent charge distribution, improved thermodynamic stability and overall water splitting.[30–32] First, Zn-ZIF-8 and Co-ZIF-8 were synthesized using two distinct approaches: a high-temperature (HT, 140 °C) solvothermal route followed by degassing at 120 °C for 12 h, yielding pZn-ZIF-8-HT and pCo-ZIF-8-HT, and a room-temperature (RT, 25 °C) aqueous method, producing pZn-ZIF-8-RT and pCo-ZIF-8-RT (details in Section 2 (SI)). Powder X-ray diffraction (PXRD) confirmed that the HT products are highly crystalline, attributable to improved thermodynamic stability, increased solubility of reactants, and faster reaction kinetics (Fig. S1b and c). In contrast, RT-synthesized samples exhibit broader and weaker PXRD peaks, reflecting lower crystallinity due to reduced solubility and slower kinetics (Fig. 1b, c and S1). Importantly, the aqueous-mediated RT synthesis represents a simple, sustainable, and environmentally friendly approach.

To generate solid solutions, mechanochemical synthesis of pZn-ZIF-8-RT and pCo-ZIF-8-RT in a 1 : 1 molar ratio was performed at 400 rpm for 2 h under an Ar atmosphere. PXRD analysis of the product revealed a broad, diffuse diffraction pattern (Fig. 1a and S1), indicative of the absence of long-range order. This structure collapse under mechanical stress resulted in the formation of an amorphous solid solution, a-

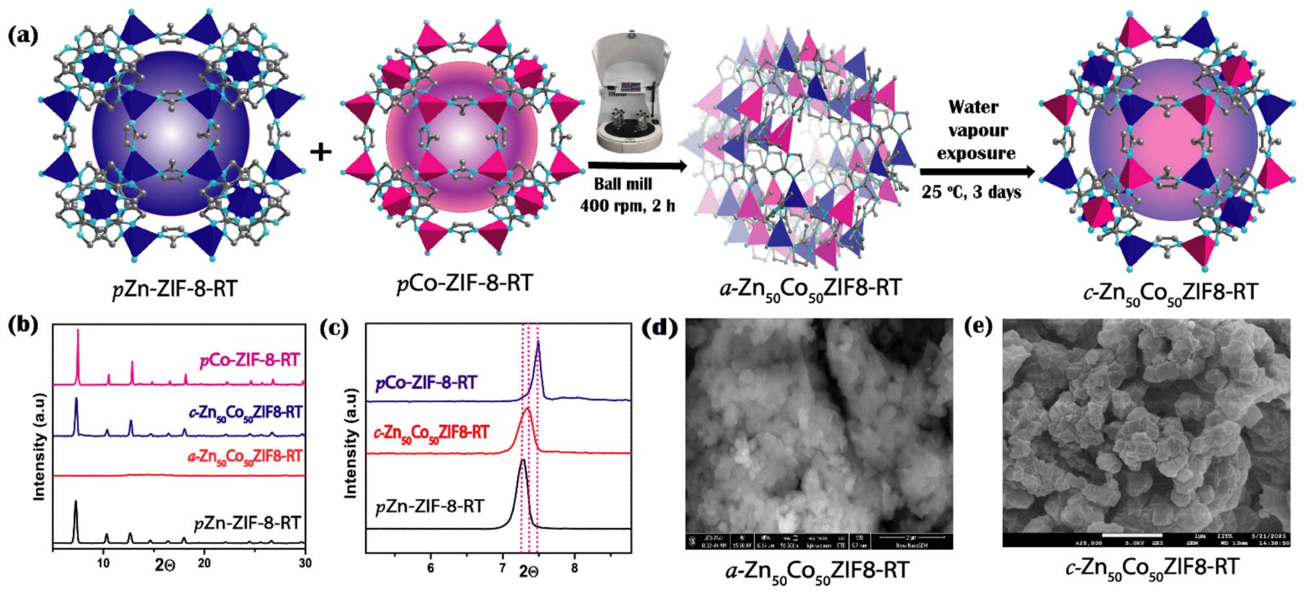

Fig. 1 (a) Schematic illustration of the synthesis of pZn-ZIF-8-RT and pCo-ZIF-8-RT *via* mechanical ball-milling followed by water-vapour exposure. (b) PXRD patterns of pZn-ZIF-8-RT, pCo-ZIF-8-RT, a-$Zn_{50}Co_{50}$ZIF8-RT, and c-$Zn_{50}Co_{50}$ZIF8-RT. (c) Zoomed version of the PXRD plot in (b) within the 2θ range from 6 to 8. (d and e) SEM images of a-$Zn_{50}Co_{50}$ZIF8-RT and c-$Zn_{50}Co_{50}$ZIF8-RT.

$Zn_{50}Co_{50}$ZIF8-RT. Upon subsequent exposure to 95% relative humidity (RH) at 25 °C for 3 days, followed by degassing at 90 °C for 12 h, the amorphous phase transformed into a crystalline solid solution, c-$Zn_{50}Co_{50}$ZIF8-RT, as evidenced by its distinct diffraction pattern compared to the pristine precursors (Fig. 1a and S1).

To further evaluate the influence of precursor crystallinity, an identical mechanochemical solid solution synthesis protocol was applied to HT-synthesized pZn-ZIF-8-HT and pCo-ZIF-8-HT. This yielded the corresponding amorphous and crystalline phases, a-$Zn_{50}Co_{50}$ZIF8-HT and c-$Zn_{50}Co_{50}$ZIF8-HT, respectively (Fig. S1b and c). PXRD confirmed that c-$Zn_{50}Co_{50}$ZIF8-HT exhibited sharp diffraction peaks distinct from its pristine frameworks (Fig. 1b and S1).[29,33] Nitrogen adsorption–desorption isotherms revealed that a-$Zn_{50}Co_{50}$ZIF8-RT possesses a very low BET surface area (21 m^2 g^{-1}), whereas its crystalline analogue, c-$Zn_{50}Co_{50}$ZIF8-RT shows a significantly higher value (402 m^2 g^{-1}, Fig. S2). Both these values are distinctly lesser when compared to pristine pZn-ZIF-8-RT (1190 m^2 g^{-1}) and pCo-ZIF-8-RT (1215 m^2 g^{-1}),[34,35] reflecting the collapse of long-range order upon prolonged milling. In contrast, the HT-derived samples exhibit higher surface areas (a-$Zn_{50}Co_{50}$ZIF8-HT: 52 m^2 g^{-1}; c-$Zn_{50}Co_{50}$ZIF8-HT:527 m^2 g^{-1}), consistent with their higher crystallinity. Pore-size distribution further revealed the coexistence of micropores (<2 nm) and mesopores (>2 nm) in all samples. However, the broader, weaker signals and higher irregularity observed in a-$Zn_{50}Co_{50}$ZIF8-RT, and to a lesser extent in c-$Zn_{50}Co_{50}$ZIF8-RT, indicate greater distortion of the pore channels compared with their HT counterparts (Fig. S3). These findings corroborate earlier reports on the reduced order of ZIF-8 structures.[29,33] Micropore analysis using the *t*-plot confirmed the reduced pore volume of a-$Zn_{50}Co_{50}$ZIF8-RT (0.0035 cm^3 g^{-1}) compared to a-$Zn_{50}Co_{50}$ZIF8-HT (0.0053 cm^3 g^{-1}, Fig. S4). Likewise, c-$Zn_{50}Co_{50}$ZIF8-RT displayed a smaller micropore volume (0.6788 cm^3 g^{-1}) than c-$Zn_{50}Co_{50}$ZIF8-HT, confirming the enhanced structural disorder in the RT-derived materials.[36]

Thermogravimetric analysis provided further insights into thermal stability: a-$Zn_{50}Co_{50}$ZIF8-HT decomposed at 498 °C, whereas a-$Zn_{50}Co_{50}$ZIF8-RT degraded at 475 °C (Fig. S5). This reduced stability of the RT sample is attributed to its highly defective, amorphous framework, in accordance with the previous observations.[36] Importantly, Fourier Transform Infrared (FT-IR) spectra confirmed the persistence of the M–N ($M = Zn^{2+}, Co^{2+}$) coordination bond at 425 cm^{-1} in both amorphous and crystalline phases after milling (Fig. S6), indicating that local coordination is well-preserved despite the global disorder.

The morphological differences between the RT- and HT-derived materials were clearly visualized by Field Emission Scanning Electron Microscope (FE-SEM) and High-Resolution Transmission Electron Microscopy (HR-TEM). FE-SEM images of a-$Zn_{50}Co_{50}$ZIF8-RT exhibited highly aggregated and irregular particles, while a-$Zn_{50}Co_{50}$ZIF8-HT displayed relatively more defined morphology. Similarly, c-$Zn_{50}Co_{50}$ZIF8-RT showed partially crystalline, fused particles, whereas c-$Zn_{50}Co_{50}$ZIF8-HT retained the characteristic rhombic dodecahedral shape observed in pristine HT-synthesized ZIFs (Fig. 1d and e).[29] Elemental mapping further confirmed the homogeneous distribution of Zn^{2+}/Co^{2+} in all samples (Fig. S7–S10).

HR-TEM provided additional evidence of disorder: a-$Zn_{50}Co_{50}$ZIF8-RT showed diffuse contrast patterns, whereas a-$Zn_{50}Co_{50}$ZIF8-HT exhibited more distinct particle boundaries (Fig. 2). For the crystalline phases, c-$Zn_{50}Co_{50}$ZIF8-RT retained the rhombic dodecahedral motif but with fused particle domains, in contrast to the well-defined crystalline morphology of c-$Zn_{50}Co_{50}$ZIF8-HT. Selected area electron diffraction (SAED) patterns further reinforced these trends: a-$Zn_{50}Co_{50}$ZIF8-RT exhibited diffuse diffraction rings with only faint spots, confirming its highly disordered atomic arrangement, while c-$Zn_{50}Co_{50}$ZIF8-HT displayed sharp diffraction spots, characteristic of an ordered crystalline lattice (Fig. S11).

Atomic absorption spectroscopy (AAS) confirmed that all solid-solution samples contained nearly equimolar Zn^{2+} and Co^{2+} ions: a-$Zn_{50}Co_{50}$ZIF8-RT (Zn: 44 mg L^{-1}, Co: 45 mg L^{-1}), c-$Zn_{50}Co_{50}$ZIF8-RT (Zn: 46 mg L^{-1}, Co: 47 mg L^{-1}), a-$Zn_{50}Co_{50}$ZIF8-HT (Zn: 48 mg L^{-1}, Co: 49 mg L^{-1}), and c-$Zn_{50}Co_{50}$ZIF8-HT (Zn: 47 mg L^{-1}, Co: 48 mg L^{-1}; Table S1, Fig. S12 and S13). These results confirm that the obtained compositions are closer to the intended 1 : 1 stoichiometry.

X-ray photoelectron spectroscopy (XPS) provided a comprehensive understanding on the oxidation states and electronic environments. The survey spectra of a-$Zn_{50}Co_{50}$ZIF8-RT and c-$Zn_{50}Co_{50}$ZIF8-RT revealed Zn, Co, C, N, and O as the major elements (Fig. S14). The Zn 2p core levels for a-$Zn_{50}Co_{50}$ZIF8-RT appeared at 1024.4 eV (Zn $2p_{3/2}$) and 1047.5 eV (Zn $2p_{1/2}$), whereas in c-$Zn_{50}Co_{50}$ZIF8-RT, both peaks shifted to slightly higher binding energies (1025.9 and 1048.8 eV), reflecting a slight shift in the local coordination environment upon crystallization.[37] The ∼23 eV splitting between Zn 2p doublets indicates the persistence of Zn^{2+} in both phases (Fig. S14c). The deconvolution of the N 1s spectra shows three major peaks. The most intense peak contributes to metal-coordinated N at

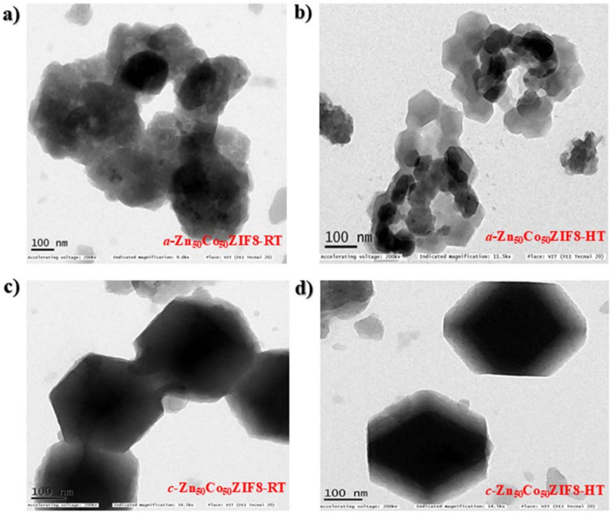

Fig. 2 HR-TEM images of (a) a-$Zn_{50}Co_{50}$ZIF8-RT, (b) a-$Zn_{50}Co_{50}$ZIF8-HT, (c) c-$Zn_{50}Co_{50}$ZIF8-RT and (d) c-$Zn_{50}Co_{50}$ZIF8-HT.

398.4 eV.[38] The peaks at 399.8 and 400.9 eV correspond to C═N and C–N, respectively (Fig. S15).[38] The Co 2p spectra displayed characteristic peaks at 783.5 and 798.7 eV (Co^{3+}, $2p_{3/2}$ and $2p_{1/2}$) along with additional peaks at 784.9 and 800.0 eV (Co^{2+}, $2p_{3/2}$ and $2p_{1/2}$), consistent with mixed Co^{2+}/Co^{3+} oxidation states. Satellite peaks were also observed at ∼784.8 and 801.1 eV with a minor positive shift in c-$Zn_{50}Co_{50}$ZIF8-RT compared to its amorphous analogue (Fig. S14d). The survey spectra of a-$Zn_{50}Co_{50}$ZIF8-HT revealed Zn, Co, C, N, and O as the major elements (Fig. S16a). The Zn 2p core levels for a-$Zn_{50}Co_{50}$ZIF8-HT appeared at 1024.8 eV (Zn $2p_{3/2}$) and 1047.7 eV (Zn $2p_{1/2}$), both peaks shifting to slightly higher binding energies (1025.9 and 1048.8 eV) compared to a-$Zn_{50}Co_{50}$ZIF8-RT, reflecting a slight shift in the local coordination environment (Fig. S16b). The Co 2p spectra displayed characteristic peaks at 783.7 and 799.6 eV (Co^{3+}, $2p_{3/2}$ and $2p_{1/2}$) along with additional peaks at 785.3 and 800.9 eV (Co^{2+}, $2p_{3/2}$ and $2p_{1/2}$), consistent with mixed Co^{2+}/Co^{3+} oxidation states. Satellite peaks were also observed at ∼789.2 and 805.5 eV, reflecting a slight shift in the local coordination environment compared to a-$Zn_{50}Co_{50}$ZIF8-RT (Fig. S16c). The presence of both Zn^{2+} and Co^{2+}/Co^{3+} in these frameworks increases metal-site heterogeneity, which can facilitate electron transfer and redox activity, the key prerequisites for efficient electrocatalysis.[39]

The chemical stability of a-$Zn_{50}Co_{50}$ZIF8-RT, c-$Zn_{50}Co_{50}$ZIF8-RT, pZn-ZIF-8-RT and pCo-ZIF-8-RT was assessed in water and various organic solvents across 25–70 °C. PXRD and FT-IR analyses (Fig. S17 and S18) confirmed that both amorphous and crystalline solid solutions retained their structural integrity under these conditions, indicating that the frameworks are chemically stable in aqueous and solvent-rich environments relevant to electrocatalytic applications (details in Section 3.2 (SI)).

Theoretical calculation

To gain deeper insights into the charge distribution, electronic configuration and structural disorder, we performed molecular cluster density functional theory (DFT) calculations on pZn-ZIF-8-RT, pCo-ZIF-8-RT, a-$Zn_{50}Co_{50}$ZIF8-RT and c-$Zn_{50}Co_{50}$ZIF8-RT. This unique theoretical approach provides a framework to rationalize how RT-synthesized precursors evolve into highly efficient amorphous and crystalline hetero-metal electrocatalysts, in contrast to those obtained from HT protocols. Notably, the computational characterization of a-$Zn_{50}Co_{50}$ZIF8-RT proved inherently more challenging owing to its lack of periodicity and symmetry. Geometry optimization of the pristine phases (pZn-ZIF-8-RT and pCo-ZIF-8-RT) and solid solutions (a-$Zn_{50}Co_{50}$ZIF8-RT and c-$Zn_{50}Co_{50}$ZIF8-RT) (Fig. S19 and S20) revealed significant differences in their electronic properties. The calculated band gaps were 5.28, 3.45, 1.11, and 1.31 eV, respectively, which are in excellent agreement with results of UV-vis DRS experiments (Fig. S20 and S21).[29] The lowest band gap of a-$Zn_{50}Co_{50}$ZIF8-RT suggests facile charge transfer and superior redox activity. Molecular electrostatic potential (MESP) plots further corroborate this, showing enhanced electron density and greater polarization in a-$Zn_{50}Co_{50}$ZIF8-RT relative to its counterparts (Fig. 3, S19c and d). Analysis of the density of states (DOS) demonstrated broad peaks around the Fermi level in a-$Zn_{50}Co_{50}$ZIF8-RT, indicating a high density of accessible energy states and thus a stronger driving force for the catalytic redox process (Fig. 3 and S21). In contrast, DOS features in a-$Zn_{50}Co_{50}$ZIF8-HT were narrower, consistent with reduced electronic activity (Fig. S21d). Theoretical thermodynamic studies further reveal that the framework in a-$Zn_{50}Co_{50}$ZIF8-RT is more densely packed and has significantly more negative ΔG (free energy) and more positive ΔS (entropy) values compared to a-$Zn_{50}Co_{50}$ZIF8-HT, which indicates that a-$Zn_{50}Co_{50}$ZIF8-RT structure is more disordered compared to a-$Zn_{50}Co_{50}$ZIF8-HT (Fig. S22a).

Raman spectra of a-$Zn_{50}Co_{50}$ZIF8-RT, a-$Zn_{50}Co_{50}$ZIF8-HT and c-$Zn_{50}Co_{50}$ZIF8-RT were analyzed theoretically as well as experimentally. Fig. S22b shows experimental bands at 190, 462, 685–720, 1145–1181 and 1145 cm^{-1} corresponding to Zn–N, Co–N, ring puckering, C–N and C–H stretching, respectively.[40,41] It is clear from the experimental plot of Raman spectra that a-$Zn_{50}Co_{50}$ZIF8-RT exhibits a very broad frequency band due to a more defective/disordered structure compared to a-$Zn_{50}Co_{50}$ZIF8-HT, and this result is close to the theoretical plot of Raman spectra, as shown in Fig. S22c. Similarly, c-$Zn_{50}Co_{50}$ZIF8-RT exhibits a more crystalline frequency band compared to a-$Zn_{50}Co_{50}$ZIF8-RT due to improved crystallinity and also aligns with the theoretical plot of Raman spectroscopy (Fig. S22b and c).

Electrochemical measurement

The distinct combination of excellent charge distribution, high electron density, thermodynamic and kinetic variations, and defect-rich frameworks prompted us to evaluate the electrocatalytic properties of ZIF-based materials toward both oxygen evolution (OER) and hydrogen evolution (HER) in alkaline medium.[42–44] Linear sweep voltammetry (LSV) reveals that a-$Zn_{50}Co_{50}$ZIF8-RT consistently outperforms all other synthesized catalysts in both the half-cell reactions (Fig. 4a and c). For the

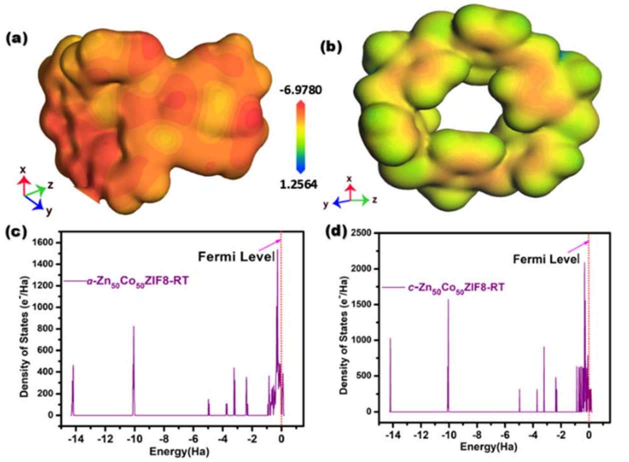

Fig. 3 Molecular electrostatic potential (MESP) mapping of (a) a-$Zn_{50}Co_{50}$ZIF8-RT and (b) c-$Zn_{50}Co_{50}$ZIF8-RT. Density of states of (c) a-$Zn_{50}Co_{50}$ZIF8-RT and (d) c-$Zn_{50}Co_{50}$ZIF8-RT.

OER, a-$Zn_{50}Co_{50}$ZIF8-RT displayed an overpotential of only 301 mV at 10 mA cm^{-2}, lower than those of c-$Zn_{50}Co_{50}$ZIF8-RT (330 mV) and pCo-ZIF-8-RT (384 mV), whereas pZn-ZIF-8-RT is essentially inactive due to its non-redox nature (Fig. 4a). Similarly, for the HER, a-$Zn_{50}Co_{50}$ZIF8-RT exhibits an overpotential of 437 mV at 10 mA cm^{-2}, outperforming that of c-$Zn_{50}Co_{50}$-ZIF8-RT (491 mV) and pCo-ZIF-8-RT (582 mV) (Table S2). Although benchmark catalysts RuO_2 (236 mV, OER) and Pt/C (70 mV, HER) showed better performance, the results obtained with a-$Zn_{50}Co_{50}$ZIF8-RT surpass those of all the other investigated ZIF-derived systems (Fig. 4b). Furthermore, the RT-derived amorphous bimetallic framework significantly outperforms most crystalline MOF/ZIF analogues reported in the literature (Tables S3 and S4). Meanwhile, the Tafel slope for the OER on a-$Zn_{50}Co_{50}$ZIF8-RT (59 mV dec^{-1}) is lower than that of RuO_2 (66.5 mV dec^{-1}). Notably, the Tafel slopes of c-$Zn_{50}Co_{50}$-ZIF8-RT (80 mV dec^{-1}) and pCo-ZIF-8-RT (94.1 mV dec^{-1}) are higher than that of a-$Zn_{50}Co_{50}$ZIF8-RT (Fig. 4c). For the HER, the Tafel slope of a-$Zn_{50}Co_{50}$ZIF8-RT (57.8 mV dec^{-1}) is not only much lower than those of c-$Zn_{50}Co_{50}$ZIF8-RT (102 mV dec^{-1}) and pCo-ZIF-8-RT (96.7 mV dec^{-1}) but also slightly lower than that of Pt/C (69.7 mV dec^{-1}), suggesting exceptionally fast reaction kinetics and a defect-rich amorphous framework of the catalyst (Fig. 4d) despite its non-noble character (Table S2).

A direct comparison of RT- and HT-derived materials clearly establishes the decisive role of the synthetic route. a-$Zn_{50}Co_{50}$-ZIF8-RT exhibits much lower overpotentials (301 mV for the OER and 437 mV for the HER) and smaller Tafel slopes (59 and 57.8 mV dec^{-1}, respectively) compared to a-$Zn_{50}Co_{50}$ZIF8-HT (400 mV and 82.4 mV dec^{-1} for the OER; 490 mV and 95 mV dec^{-1} for the HER), as shown in Fig. S23. The enhanced bifunctional performance of the RT-derived sample originates from the greater disorder and defect density imparted during mechanochemical milling, which generates abundant active sites and facilitates electron transfer. The inherent activity of the catalysts was further probed by evaluating the turnover frequency (TOF), double-layer capacitance (C_{dl}) and electrochemical active surface area (ECSA). Among all tested systems, a-$Zn_{50}Co_{50}$ZIF8-RT exhibits the highest TOF value of 3.6×10^{-3} s^{-1} for the HER and 35.2×10^{-3} s^{-1} for the OER. The C_{dl} values were calculated by performing CV at different scan rates and by plotting the anodic and cathodic current slopes at the middle potential (Fig. S25 and S26). a-$Zn_{50}Co_{50}$ZIF8-RT exhibited a C_{dl} value of 0.618 mF and the largest ECSA (15.45 cm^2), corroborating its superior intrinsic activity (Fig. S24a, b and Table S2, Section 5.1). Together, these results establish a-$Zn_{50}Co_{50}$ZIF8-RT as an efficient bifunctional electrocatalyst for water splitting, in which the synergistic interplay of Zn/Co heterometallic states, defect-rich amorphous architecture, and optimized electronic structure drives both the OER and HER with remarkable efficiency. In addition, to examine the charge transport characteristics, EIS measurements were performed in the frequency range from 100 Hz to 1000 kHz. Fig. S27 shows the Nyquist plot of all the synthesized materials, which was fitted using the circuit given as an inset in Fig. S27. The Nyquist plots reveal that a-$Zn_{50}Co_{50}$ZIF8-RT exhibits a significantly lower transfer resistance (R_{ct}) of 0.77 Ω compared to c-Zn_{50}-Co_{50}ZIF8-RT (1.16 Ω), a-$Zn_{50}Co_{50}$ZIF8-HT (3.32 Ω), c-$Zn_{50}Co_{50}$-ZIF8-HT (4.81 Ω), pCo-ZIF8-RT (2.13 Ω) and pZn-ZIF8-RT (10.64 Ω), confirming faster interfacial electron transfer and supporting the observed enhanced kinetics.

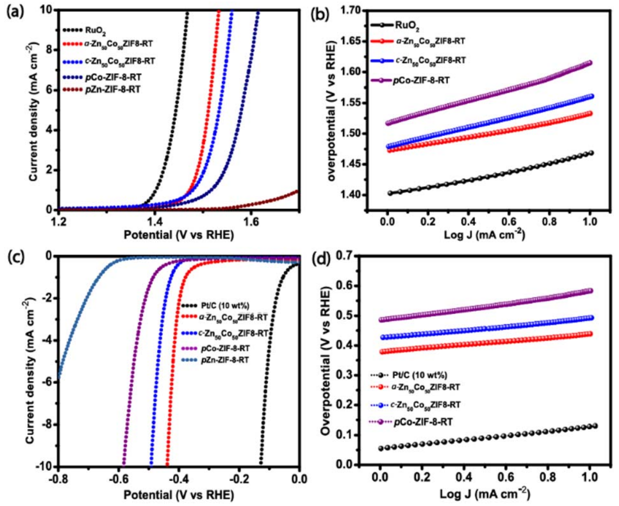

Fig. 4 Electrochemical performance of the catalysts: (a) linear sweep voltammetry (LSV) curves and (b) Tafel slopes for oxygen evolution reaction (OER). (c) LSV curves and (d) Tafel slopes for hydrogen evolution reaction (HER) of all catalysts at a current density of 10 mA cm^{-2}.

The electrocatalytic water splitting and the stability of the electrocatalyst were demonstrated using a two-electrode system, as shown in Fig. S28, Section 5.2. The chronoamperometry measurement was performed at an applied cell potential of 1.97 V for a-$Zn_{50}Co_{50}$ZIF8-RT and 2.05 V for c-$Zn_{50}Co_{50}$ZIF8-RT, as shown in Fig. S29. This was compared with various previously reported MOF-based electrocatalysts for overall water splitting, as shown in Table S5. Both the electrode materials show a stable current response at 10 mA cm^{-2} with a negligible change in current at the corresponding applied potential, as shown in Fig. S29. These results confirm that a-$Zn_{50}Co_{50}$ZIF8-RT requires a cell potential of less than 2 V; thus, this material can be implemented in the real-time application for overall water splitting. Furthermore, chronoamperometry was also performed at a fixed potential at 50 mA cm^{-2} current density, as shown in Fig. S30, Section 5.3. The chronoamperometric curve shows a stable current response at a fixed potential for 48 h. Thus, the results obtained suggest the excellent long-term stability of a-$Zn_{50}Co_{50}$ZIF8-RT even at a higher current density.

To probe the structural integrity after prolonged electrolysis, the a-$Zn_{50}Co_{50}$ZIF8-RT catalyst was examined by PXRD, FT-IR, STEM, Raman and ICP-MS. As discussed earlier, instability assessment was done by PXRD, and a-$Zn_{50}Co_{50}$ZIF8-RT displayed a broad and diffuse diffraction pattern (Fig. 1b). In contrast, the crystalline c-$Zn_{50}Co_{50}$ZIF8-RT retained its well-defined reflections even after chronoamperometric operation in 1 M KOH at 25 °C for up to 10 h (Fig. S31), indicating its excellent structural robustness under OER and HER conditions. Complementarily, FT-IR analysis of a-$Zn_{50}Co_{50}$ZIF8-RT revealed that all characteristic vibrational bands persisted after identical testing periods (1, 2, and 10 h; Fig. S32), further confirming that both amorphous and crystalline Zn/Co-ZIFs retained their structural motifs during catalysis. STEM provided additional evidence of pre- and post-catalytic study of a-$Zn_{50}Co_{50}$ZIF8-RT. Elemental mapping of *a*-$Zn_{50}Co_{50}$ZIF8-RT pre- and post-catalytic study further confirmed the homogeneous distribution of Zn^{2+}/Co^{2+} in it, as shown in Fig. S33 and S34. Raman spectra of a-$Zn_{50}Co_{50}$ZIF8-RT were also obtained before and after the catalytic study. Fig. S35 shows experimental bands at 191 and 466 cm^{-1} corresponding to Zn–N and Co–N stretching. This confirmed that its structure is still intact post-catalytic study. We also performed ICP-MS of a-$Zn_{50}Co_{50}$ZIF8-RT before and after a prolonged electrochemical stability study. Fig. S36 clearly indicates that Zn^{2+} and Co^{2+} are in equal ratio before and after the catalytic study. These results indicate that the a-$Zn_{50}Co_{50}$ZIF8-RT catalyst maintain its compositional integrity after the stability test.

Conclusions

This study demonstrates the decisive role of the synthetic protocol in dictating the structure–property relationship of mechanochemical synthesis of Zn/Co-ZIF-8 solid solutions. Water-mediated RT synthesis followed by mechanochemical milling yields a highly disordered amorphous phase (a-$Zn_{50}Co_{50}$ZIF8-RT), which upon vapor treatment transforms into a crystalline analogue (c-$Zn_{50}Co_{50}$ZIF8-RT). In contrast, HT-derived precursors produce more ordered frameworks compared to RT derived compounds. Comprehensive experimental and theoretical analyses reveal that the defect-rich amorphous a-$Zn_{50}Co_{50}$ZIF8-RT exhibits enhanced electron density, abundant active sites, and superior charge-transfer characteristics, resulting in excellent electrocatalytic activity with overpotentials of 301 mV (OER) and 437 mV (HER) at 10 mA cm^{-2}, outperforming both crystalline and HT-derived counterparts. These findings establish structural disorder, induced by water-mediated mechanochemistry, as a powerful design principle for advancing heterometallic MOF/ZIF electrocatalysts in energy conversion. Looking ahead, this strategy offers a broadly applicable platform towards engineering defect-rich, heterometallic frameworks for next-generation electrolyzers and sustainable hydrogen generation technologies.

Conflicts of interest

There are no conflicts to declare.

Data availability

All relevant data supporting this article have been included within the article and its supplementary information (SI) files. Additional raw data can be provided by the corresponding author upon reasonable request. Supplementary information is available. See DOI: https://doi.org/10.1039/d6ta00038j.

Acknowledgements

This work was carried out with financial assistance from the Science and Engineering Research Board (SERB), Government of India, through a start-up research grant SRG/2020/001108. P. K. acknowledges the CSIR-HRDG India for the SRF.

References

1 (*a*) Y. Zheng, Y. Jiao, A. Vasileff and S.-Z. Qiao, *Angew. Chem., Int. Ed.*, 2018, **57**, 7568–7579; (*b*) C. Zhang, Y. Huang, Y. Yu, J. Zhang, S. Zhuo and B. Zhang, *Chem. Sci.*, 2017, **8**, 2769–2775; (*c*) Y. Chen, G. Yu, W. Chen, Y. Liu, G.-D. Li, P. Zhu, Q. Tao, Q. Li, J. Liu, X. Shen, H. Li, X. Huang, D. Wang, T. Asefa and X. Zou, *J. Am. Chem. Soc.*, 2017, **139**, 12370–12373.
2 Z. Wu, X. Guo, Z. Zhang, M. Song, T. Jiao, Y. Zhu, J. Wang and X. Liu, *ACS Sustainable Chem. Eng.*, 2019, **7**, 16577–16584.
3 M. Song, Z. Zhang, Q. Li, W. Jin, Z. Wu, G. Fu and X. Liu, *J. Mater. Chem. A*, 2019, **7**, 3697–3703.
4 N.-T. Suen, S.-F. Hung, Q. Quan, N. Zhang, Y.-J. Xu and H. M. Chen, *Chem. Soc. Rev.*, 2017, **46**, 337–365.
5 H. S. Jadhav, A. Roy, G. M. Thorat, W.-J. Chung and J. G. Seo, *J. Ind. Eng. Chem.*, 2019, **71**, 452–459.
6 X. Xiao, D. Huang, Y. Fu, M. Wen, X. Jiang, X. Lv, M. Li, L. Gao, S. Liu, M. Wang, C. Zhao and Y. Shen, *ACS Appl. Mater. Interfaces*, 2018, **10**, 4689–4696.
7 A. R. Jadhav, J. M. C. Puguan and H. Kim, *ACS Sustainable Chem. Eng.*, 2017, **5**, 11069–11079.
8 S. Zheng, X. Guo, H. Xue, K. Pan, C. Liu and H. Pang, *Chem. Commun.*, 2019, **55**, 10904–10907.
9 S. Shit, S. Chhetri, W. Jang, N. C. Murmu, H. Koo, P. Samanta and T. Kuila, *ACS Appl. Mater. Interfaces*, 2018, **10**, 27712–27722.
10 F. Yu, H. Zhou, Y. Huang, J. Sun, F. Qin, J. Bao, W. A. Goddard, S. Chen and Z. Ren, *Nat. Commun.*, 2018, **9**, 2551.
11 V. K. Abdelkader-Fernández, D. M. Fernandes, S. S. Balula, L. Cunha-Silva and C. Freire, *J. Mater. Chem. A*, 2020, **8**, 13509–13521.
12 W. Wu, Z. Zhang, Z. Lei, X. Wang, Y. Tan, N. Cheng and X. Sun, *ACS Appl. Mater. Interfaces*, 2020, **12**, 10359–10368.
13 (*a*) G. Jia, W. Zhang, G. Fan, Z. Li, D. Fu, W. Hao, C. Yuan and Z. Zou, *Angew. Chem., Int. Ed.*, 2017, **56**, 13781–13785; (*b*) P. Kumari, A. Kareem, P. Jhariat, S. Senthilkumar and T. Panda, *Inorg. Chem.*, 2023, **62**, 3457–3463.
14 H. Bux, F. Y. Liang, Y. S. Li, J. Cravillon, M. Wiebcke and J. Caro, *J. Am. Chem. Soc.*, 2009, **131**, 16000–16001.
15 K. H. Li, D. H. Olson, J. Seidel, T. J. Emge, H. W. Gong, H. P. Zeng and J. Li, *J. Am. Chem. Soc.*, 2009, **131**, 10368–10369.
16 S. R. Venna and M. A. Carreon, *J. Am. Chem. Soc.*, 2010, **132**, 76–78.
17 E. C. Spencer, R. J. Angel, N. L. Ross, B. E. Hanson and J. A. K. Howard, *J. Am. Chem. Soc.*, 2009, **131**, 4022–4026.

18 K. S. Park, Z. Ni, A. P. Côté, J. Y. Choi, R. Huang, F. J. Uribe-Romo, H. K. Chae, M. O'Keeffe and O. M. Yaghi, *Proc. Natl. Acad. Sci. U. S. A.*, 2006, **103**, 10186–10191.

19 Q. Shi, Z. Chen, Z. Song, J. Li and J. Dong, *Angew. Chem., Int. Ed.*, 2011, **50**, 672–675.

20 (*a*) C. P. Li and M. Du, *Chem. Commun.*, 2011, **47**, 5958–5972; (*b*) K. Kida, M. Okita, K. Fujita, S. Tanaka and Y. Miyake, *CrystEngComm*, 2013, **15**, 1794–1801; (*c*) H. Ghorbani, M. Ghahramaninezhad and M. N. Shahrak, *J. Solid State Chem.*, 2020, **289**, 1–8.

21 H. S. Jadhav, H. A. Bandal, S. Ramakrishna and H. Kim, *Adv. Mater.*, 2022, **34**, 1–74.

22 (*a*) D. Sun, D. Yang, P. Wei, B. Liu, Z. Chen, L. Zhang and J. Lu, *ACS Appl. Mater. Interfaces*, 2020, **12**, 41960–41968; (*b*) M. Zhong, L. Kong, K. Zhao, Y. Zhang, N. Li and X. Bu, *Adv. Sci.*, 2021, **8**, 2001980; (*c*) V. Armel, J. Hannauer and F. Jaouen, *Catalysts*, 2015, **5**, 1333–1351.

23 M. J. V. Vleet, T. Weng, X. Li and J. R. Schmidt, *Chem. Rev.*, 2018, **118**, 3681–3721.

24 Y. Pan, Y. Liu, G. Zeng, L. Zhao and Z. Lai, *Chem. Commun.*, 2011, **47**, 2071–2073.

25 S. Wu, M. Li and Y. Sun, *Angew. Chem., Int. Ed.*, 2019, **58**, 8987–8995.

26 H. Bunzen, M. Grzywa, M. Hambach, S. Spirkl and D. Volkmer, *Cryst. Growth Des.*, 2016, **16**, 3190–3197.

27 S. J. Baxter, A. Schneemann, A. D. Ready, P. Wijeratne, A. P. Wilkinson and N. C. Burtch, *J. Am. Chem. Soc.*, 2019, **141**, 12849–12854.

28 G. Kaur, R. K. Rai, D. Tyagi, X. Yao, P. Z. Li, X. C. Yang, Y. Zhao, Q. Xu and S. K. Singh, *J. Mater. Chem. A*, 2016, **4**, 14932–14938.

29 P. Kumari and T. Panda, *Inorg. Chem.*, 2023, **62**, 15335–15339.

30 M. R. Kandel, U. N. Pan, P. P. Dhakal, R. B. Ghising, S. Sidra, D. H. Kim, N. H. Kim and J. H. Lee, *Small*, 2024, **20**, 2307241.

31 M. R. Kandel, U. N. Pan, P. P. Dhakal, R. B. Ghising, T. T. Nguyen, J. Zhao, N. H. Kim and J. H. Lee, *Appl. Catal., B*, 2023, **331**, 122680.

32 U. N. Pan, M. R. Kandel, A. K. Tomar, N. H. Kim and J. H. Lee, *Small*, 2024, **20**, 2305519.

33 T. Panda, S. Horike, K. Hagi, N. Ogiwara, K. Kadota, T. Itakura, M. Tsujimoto and S. Kitagawa, *Angew. Chem.*, 2017, **129**, 2453–2457.

34 R. R. Kuruppathparambil, R. Babu, H. M. Jeong, G. Y. Hwang, G. S. Jeong, M. Il Kim, D. W. Kim and D. W. Park, *Green Chem.*, 2016, **18**, 6349–6356.

35 G. Kaur, R. K. Rai, D. Tyagi, X. Yao, P.-Z. Li, X.-C. Yang, Y. Zhao, Q. Xu and S. K. Singh, *J. Mater. Chem. A*, 2016, **4**, 14932–14938.

36 S. Cao, T. D. Bennett, D. A. Keen, A. L. Goodwin and A. K. Cheetham, *Chem. Commun.*, 2012, **48**, 7805–7807.

37 (*a*) X. Yang, J. Zhang, X. Tian, J. Qin, X. Zhang and L. Ma, *Angew. Chem.*, 2023, **135**, e202216699; (*b*) P. Z. Li, K. Aranishi and Q. Xu, *Chem. Commun.*, 2012, **48**, 3173–3175.

38 (*a*) O. Abuzalat, H. Tantawy, M. Basuni, M. H. Alkordi and A. Barakaa, *RSC Adv.*, 2022, **12**, 6025–6036; (*b*) Y. Jiang, Y. Lu, X. Wang, Y. Bao, W. Chena and L. Niu, *Nanoscale*, 2014, **6**, 15066–15072; (*c*) G. Wu, C. M. Johnston, N. H. Mack, K. Artyushkova, M. Ferrandon, M. Nelson, J. S. Lezama-Pacheco, S. D. Conradson, K. L. More and D. J. Myersd, *J. Mater. Chem.*, 2011, **21**, 11392–11405.

39 (*a*) H. Wen, S. Zhang, T. Yu, Z. Yi and R. Guo, *Nanoscale*, 2021, **13**, 12058–12087; (*b*) M. Chafiq, A. Chaouiki, T. Suhartono and Y. G. Ko, *J. Mater. Chem. A*, 2023, **11**, 23984–23998.

40 (*a*) S. Chen, X. Li, E. Dong, H. Lv, X. Yang, R. Liu and B. Liu, *J. Phys. Chem. C*, 2019, **123**, 29693–29707; (*b*) D. Radhakrishnan and C. Narayana, *J. Chem. Phys.*, 2016, **144**, 4–10.

41 S. Hajra, M. Sahu, A. M. Padhan, J. Swain, B. K. Panigrahi, H. G. Kim, S. W. Bang, S. Park, R. Sahu and H. J. Kim, *J. Mater. Chem. C*, 2021, **9**, 17319–17330.

42 F. Guo, M. Zhang, S. Yi, X. Li, R. Xin, M. Yang, B. Liu, H. Chen, H. Li and Y. Liu, *Nano Res. Energy*, 2022, **1**, 9120027.

43 T. Wang, Y. He, Y. Liu, F. Guo, X. Li, H. Chen, H. Li and Z. Lin, *Nano Energy*, 2021, **79**, 105487.

44 T. Wang, C. Yang, Y. Liu, M. Yang, X. Li, Y. He, H. Li, H. Chen and Z. Lin, *Nano Lett.*, 2020, **20**, 5639–5645.